Research Article | Vol. 30, No. 7 / 28 Mar 2022 / Optics Express 12092
Optics EXPRESS

All-dielectric multi-resonant bullseye antennas

AMY BUTCHER[1] AND ALEXANDER A. HIGH[1,2,*]

[1] Pritzker School of Molecular Engineering, University of Chicago, Chicago, IL 60615, USA
[2] Center for Molecular Engineering and Materials Science Division, Argonne National Laboratory, Lemont, IL 60439, USA
[*] ahigh@uchicago.edu

Abstract: Integrated devices that generate multiple optical resonances in the same volume can enhance on-chip nonlinear frequency generation, nonlinear spectroscopy, and quantum sensing. Here, we demonstrate circular Bragg antennas that exhibit multiple spatially overlapping, polarization-selective optical resonances. Using templated atomic layer deposition of TiO_2, these devices can be fabricated on arbitrary substrates, making them compatible with a wide range of nonlinear materials and sensing targets, and couple efficiently to underlying films. In this work, we detail the design, simulation, and fabrication of all-dielectric multi-resonant bullseye antennas and characterize their performance using polarized broadband reflection spectroscopy.

1. Introduction

By confining and enhancing optical fields at pre-designed wavelengths, nanophotonic resonators enable coherent light-matter interactions [1,2], ultra-resolution quantum and bio-sensing [3,4], integrated light sources [5,6], and more. Nonlinear light-matter interactions underly on-chip nonlinear frequency conversion, critical for entangled photon sources and optical information processing [7–11], and are enhanced by devices which spatially overlap multiple optical resonances at different frequencies. Similarly, coherent anti-Stokes Raman spectroscopy and other nonlinear spectroscopies can be made more efficient and extended to smaller probe volumes by simultaneously confining the pump and signal frequencies [12,13]. Meanwhile, in optical sensing applications, multi-resonant structures can increase optical pumping efficiency while simultaneously increasing fluorescence emission rates [13,14].

However, generating devices which overlap multiple optical resonances at arbitrary frequencies is challenging, both in terms of design and fabrication. Many nanophotonic resonators rely on photonic band gap engineering, in which a resonance exists within forbidden photonic states. Although multiple resonances can exist within one band gap, their frequency separation is constrained by the width of the photonic band gap, and it is difficult to independently control the field strength and quality factors of the resonant modes. Ring resonators, meanwhile, do not rely on band gap engineering, support a series of standing wave resonances, and are generally easier to fabricate than photonic crystals. These devices are commonly used for on-chip nonlinear frequency generation and for sensing [8,15–17], though their disadvantages include larger footprints and mode volumes than photonic crystal cavities. For nonlinear applications, a key challenge is that the cross-sectional spatial profiles of ring resonator modes vary with wavelength, and careful engineering of waveguide cross sections is often required to enable substantial mode overlap [18,19].

Alternatively, circular Bragg resonators (CBRs), also called bullseye antennas, offer unique benefits for nanophotonic engineering. These structures efficiently couple to low-NA far-field beams and exhibit smaller mode volumes and footprints than ring resonators [20–26]. Additionally, CBRs offer a relatively broadband optical response and are therefore easier to spectrally overlap with targeted dipole emission. CBRs were initially used for classical optoelectronic devices like optical switches and lasers [20–22]. More recently, they have been integrated with a variety

#455232 https://doi.org/10.1364/OE.455232
Journal © 2022 Received 31 Jan 2022; revised 10 Mar 2022; accepted 12 Mar 2022; published 25 Mar 2022

Optics EXPRESS

of quantum and low-dimensional materials. CBRs have been etched into diamond membranes to increase collection efficiency of nitrogen-vacancy center emission [23], used to efficiently extract entangled photon pairs from quantum dots [24], and integrated with two-dimensional semiconductors to enhance photoluminescence and second harmonic generation [25,26].

Breaking azimuthal symmetry allows multiple resonances in CBRs while maintaining their unique advantages. This symmetry breaking enables both wavelength and polarization multiplexing, as segments with different grating periods behave like polarization-selective antennas. This concept was demonstrated in plasmonic CBRs fabricated by focused ion beam milling of epitaxially grown single-crystal silver [27]. However, plasmonic devices suffer from large nonradiative losses compared to dielectric structures. Moreover, silver epitaxy and ion milling offer limited integration capability with many nonlinear materials.

In this work, we use templated atomic layer deposition (ALD) to build all-dielectric TiO_2 bullseye antennas which exhibit multiple polarization-sensitive, spatially overlapping resonances. We previously demonstrated that this fabrication approach can efficiently couple nanophotonic devices with underlying materials and can be integrated with arbitrary substrates [28]. Specifically, templated ALD maintains the optical performance of underlying 2D materials [29] and is uniquely suited for integration with quantum emitters in membranes [28,30]. Here, we detail the design, fabrication, and spectroscopic characterization of multi-resonant TiO_2 bullseye antennas and demonstrate their potential to interface with underlying optical materials.

2. Device design and simulation

2.1. Device geometry and operating principle

Circular Bragg resonators (CBRs) typically feature a central disk concentric with periodically spaced rings. The rings are spaced according to the second order Bragg condition and serve the dual function of reflective feedback to the central cavity and deflection out-of-plane, thereby coupling the cavity mode to low-NA propagating beams. With quality factors on the order of 10^2, these devices offer a relatively broadband response (several nm), combined with a small footprint (< 5 um) and mode volume ($\sim (\lambda/n)^3$). Variations on this basic geometry that have previously been explored include chirped cavities for high-Q applications [31], elliptical cavities for geometric birefringence [24], and Doppler gratings for wavelength multiplexing [12].

For the azimuthally segmented, multi-resonant devices we designed, the operating mechanism is the same as that of basic CBRs, except each segment has its own central disc radius and grating pitch. The structure is symmetric about its center, with each grating pitch repeated on the opposite side of the device. As illustrated in Fig. 1(a), these devices can be defined by six parameters: a_1 and a_2 are the two grating periods, R_1 and R_2 are the corresponding central disc radii, and θ_1 and θ_2 define the angular spread of each segment, with $\theta_1 + \theta_2 = 180°$.

To demonstrate the potential of multi-resonant bullseye antennas to interface with underlying materials, we used finite difference time domain (FDTD) simulations (Lumerical) to model devices on 50 nm TiO_2 films on fused silica (n = 1.4) substrates, as depicted in Fig. 1(b). Because the index of refraction of TiO_2 is close to that of lithium niobate (n ~ 2.3), diamond (n ~ 2.4), silicon carbide (n ~ 2.6), and hexagonal boron nitride (n ~ 2.2), this substrate choice is a suitable stand-in for materials relevant to a range of practical applications in nonlinear and quantum optics. We note that the resonator modes are concentrated within the bullseye antenna and in the film directly underneath, as shown in Figs. 1(c) and 1(d), in contrast to zone plates or metalenses which are often used to focus an incident beam to a point away from the structure itself [32].

We identified device parameters that concentrated multiple resonances within the underlying film by linearly varying the two grating periods and disc radii and monitoring the electric field intensity underneath the resonator [33]. In all simulations, the height of the devices was fixed at 300 nm, and the index of refraction of TiO_2 was input from ellipsometry data [28,33]. Additionally, the duty cycle of each grating was set such that the width of each grating element

Optics EXPRESS

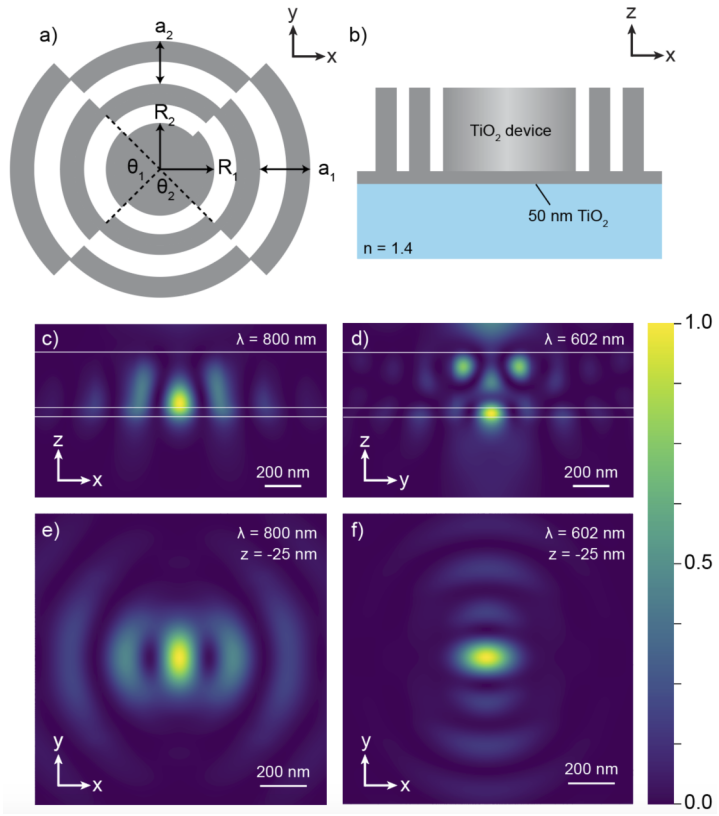

Fig. 1. Multi-resonant device design. (a) The geometrical parameters that define the device are the radius of the central disc segment for each resonance (R_1, R_2), the corresponding pitch values (a_1, a_2), and the angles subtended by each segment (θ_1, θ_2, where $\theta_1 + \theta_2 = 180°$). (b) Side view of the simulated device and substrate. (c, d) Simulated electric field intensity in the x-z and y-z planes for a device with resonances at 800 nm (c) and 602 nm (d) on a 50 nm TiO_2 film. (e, f) Simulated electric field intensity in the x-y plane at the center of the underlying film ($z = -25$ nm) for each of the two resonances, demonstrating substantial mode overlap. All field intensity plots are normalized.

was equal to the grating period divided by 2.1. Once resonance conditions were identified, we found that each resonant wavelength varies linearly with small changes to either the central disc radius or the grating period. However, a large variation in one of these parameters generally leads to a loss of the resonance condition without a compensating adjustment in the other [33]. We therefore identified a series of pairs of parameters that yielded strong resonances to explore further. This design process, which relies on individual variable sweeps, can likely be further optimized using field-based or inverse design methods [34,35].

In Figs. 1(e) and 1(f), we plot the in-plane electric field intensity profiles underneath ($z = -25$ nm) a device with parameters (a_1, R_1, a_2, R_2) = (179, 212, 233, 248) nm, which generates resonances at both 800 and 602 nm. These results demonstrate substantial mode overlap at the center of the underlying film, even for wavelengths separated by nearly 200 nm [33].

2.2. Simulated incident beam enhancement

To investigate the polarization selectivity of the multi-resonant TiO_2 bullseye antennas, we simulated a focused, linearly polarized Gaussian beam normally incident on the center of the

Optics EXPRESS

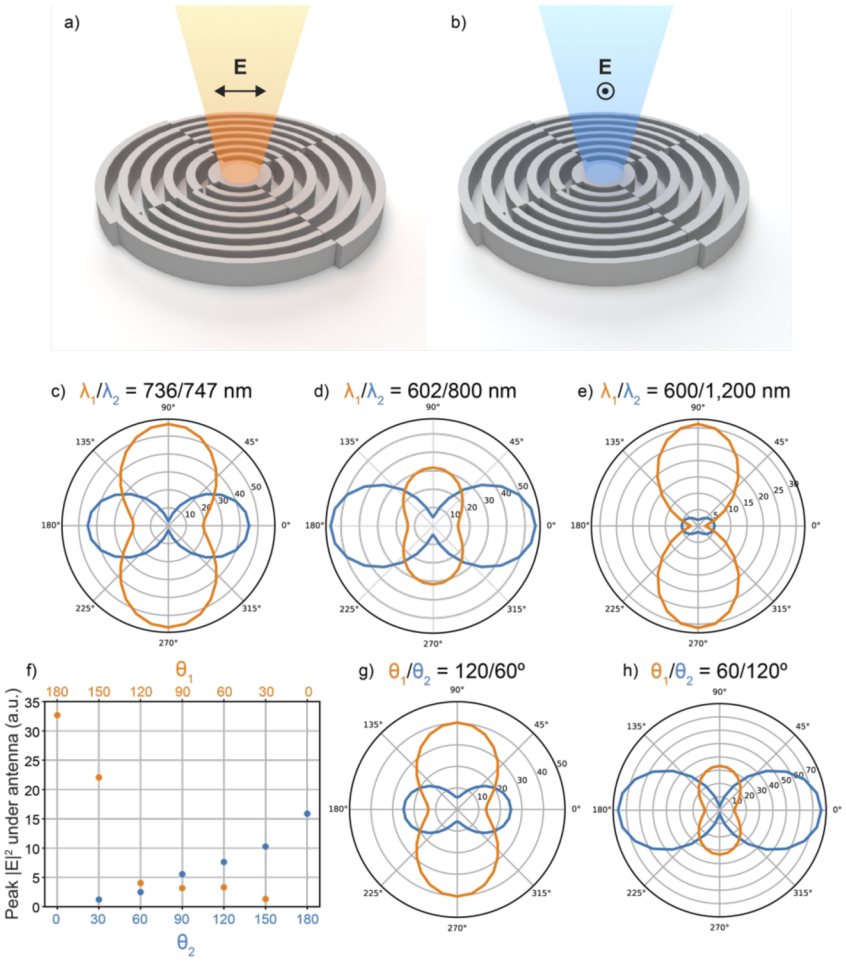

Fig. 2. Incident beam intensity enhancement. (a, b) Incident beams polarized in the x-direction (a) and in the y-direction (b) preferentially couple to different resonances in the azimuthally segmented bullseyes. (c-e) Simulated electric field intensity in the film underneath the devices ($z = -25$ nm) as a function of incident beam polarization for different combinations of resonances. In these three plots, $\theta_1 = \theta_2 = 90°$. (f) Peak electric field intensity in the underlying film for the same device as in (d) as a function of θ_1 and θ_2. (g, h) Electric field intensity ($z = -25$ nm) versus beam polarization for $\theta_1 = 120°$ (g) and $\theta_1 = 60°$ (h). In these two plots, the other device parameters (a_1, R_1, a_2, R_2) are the same as in (d) and (f).

device and varied its polarization angle. Figures 2(a) and 2(b) illustrate that perpendicularly polarized beams couple selectively to one resonance or the other. Imagining a line that passes through the center of a particular grating segment, a beam polarized perpendicular to that line will couple most effectively to the resonance defined by that segment. In the illustration, the orange (blue) beam preferentially couples to the shorter (longer) pitch grating.

We recorded the simulated electric field intensity at the center of the TiO_2 film underneath the bullseye resonator ($z = -25$ nm) as the beam source polarization was varied. Figures 2(c)-(e) plot in polar coordinates the intensity enhancement at the two resonant wavelengths of a given device as a function of beam polarization angle. All three of the dual resonance devices demonstrated here display clear polarization selectivity, regardless of the spectral separation of the two primary

Optics EXPRESS

resonances. These devices demonstrate that the multi-resonant bullseyes can be designed for two wavelengths that are relatively close together (Fig. 2(c)), several hundred nm apart (Fig. 2(d)) or even for fundamental and second harmonic wavelengths (Fig. 2(e)).

Varying the angle subtended by each segment of the device offers a method of tuning the relative intensity of the two resonances. Figure 2(f) demonstrates that as θ_1 (θ_2) is increased (decreased) the shorter wavelength resonance becomes more (less) intense and vice versa. Importantly, even when θ_1 and θ_2 are not 90°, the device retains its selectivity to orthogonal polarizations, as shown in Fig. 2(g) and 2(h).

2.3. Simulated dipole emission enhancement and out-coupling profile

Next, using a point dipole source located in the center of the underlying film (z = −25 nm), we simulated the Purcell enhancement and far field emission profiles generated by the multi-resonant Bragg antennas. Like the case of an incident polarized beam, underlying dipoles with orthogonal, in-plane dipole moments (x or y) couple selectively to different resonances in the device, as illustrated in Fig. 3(a) and 3(b). Purcell factors were extracted directly from simulations using the built-in Lumerical FDTD analysis, which calculates these values based on the local density of optical states at the dipole position.

For each simulated device, we recorded the Purcell factor for dipole emission at the two resonant wavelengths as a function of the dipole orientation angle. Figures 3(c)-(e) plot these results in polar coordinates for the same devices that were investigated in Figs. 2(c)-(e), each with $\theta_1 = \theta_2 = 90°$. As expected, the Purcell factor for underlying dipoles displays a similar polarization selectivity as the intensity of incident beams displayed in the prior set of simulations. Likewise, varying the angle subtended by each resonance modulates the degree of dipole emission enhancement at the two resonant wavelengths. As θ_1 (θ_2) is increased (decreased) the shorter wavelength dipole is more (less) enhanced and vice versa. Here, the Purcell enhancement achieved by single resonance devices (θ_1 or $\theta_2 = 180°$) is in the range 10–20, which is similar to previous work investigating dipole emission enhancement by CBRs [23], despite the fact that these dipoles are underneath rather than inside of the device itself. Finally, we again see that when θ_1 and θ_2 are not 90°, the device retains its selectivity to orthogonal polarizations, as shown in Figs. 3(g) and 3(h).

To test if the azimuthally segmented devices efficiently couple dipole emission into low-NA far field modes like single resonance CBRs, we investigated the spatial distribution of emission from underlying dipoles. For these simulations, we analyzed a device with resonances at 799 and 598 nm and considered emission profiles of dipoles oriented in the x- and y-directions that were on resonance with these two wavelengths. The dipoles were again placed in the center of the TiO_2 film under the antenna (z = −25 nm) and the device angles were $\theta_1 = \theta_2 = 90°$.

The cross-sectional electric field intensity profiles, plotted in Figs. 4(a) and 4(b) with a $\log_{10}$ scale, demonstrate that dipole emission is significantly vertical, in both the upward (+z) and downward (-z) directions. This vertical characteristic is evident for both x-oriented and y-oriented dipoles at the appropriate resonance wavelength. Because the simulated substrate has a higher index of refraction (n = 1.4) than the surrounding medium (n = 1.0), more radiation is emitted downwards than upwards. Nevertheless, 41% of emission from an x-oriented dipole at 799 nm and 27% from a y-oriented dipole at 598 nm is directed upward [33].

Figures 4(c) and 4(d) display the far field projections of upward dipole emission. While the emission profiles are not Gaussian, the emission of an x-oriented (y-oriented) dipole at the shorter (longer) wavelength resonance is primarily concentrated with NA = 0.75. In applications where collection efficiency is paramount, such as in quantum sensing, objectives with numerical apertures in air of up to 0.9 are commonly used and can therefore collect nearly the full upward emission from dipoles coupled to these multi-resonant devices. Combined with Purcell enhancement, we

Optics EXPRESS

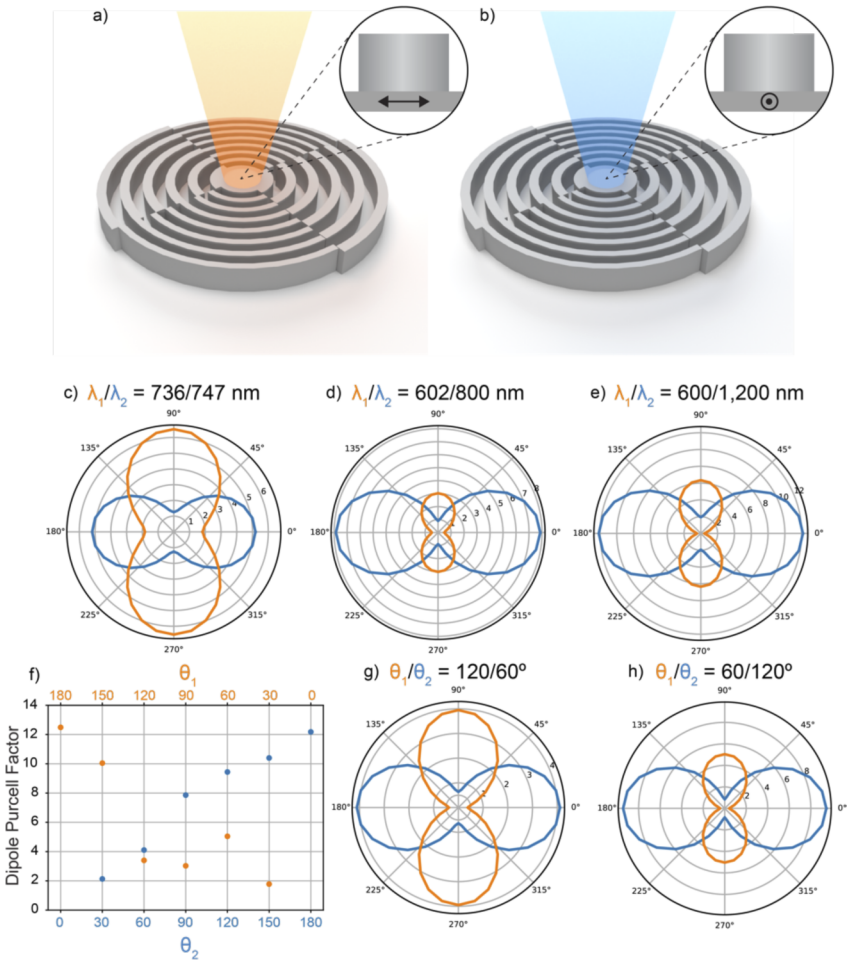

Fig. 3. Dipole Purcell enhancement. (a, b) Dipoles with moments in the x-direction (a) and in the y-direction (b) preferentially couple to different resonances in the azimuthally segmented bullseyes. (c-e) Simulated Purcell factor for a dipole in the center underneath the devices (z = −25 nm) as a function of dipole orientation for different combinations of resonances. In these three plots, $\theta_1 = \theta_2 = 90°$. (f) Peak Purcell factor for underlying dipoles for the same device as in (d) as a function of θ_1 and θ_2. (g, h) Purcell factor (z = −25 nm) versus dipole orientation for $\theta_1 = 120°$ (g) and $\theta_1 = 60°$ (h). In these two plots, the other device parameters (a_1, R_1, a_2, R_2) are the same as in (d).

can expect multi-resonant bullseye antennas to significantly increase experimental collection efficiency.

Optics EXPRESS

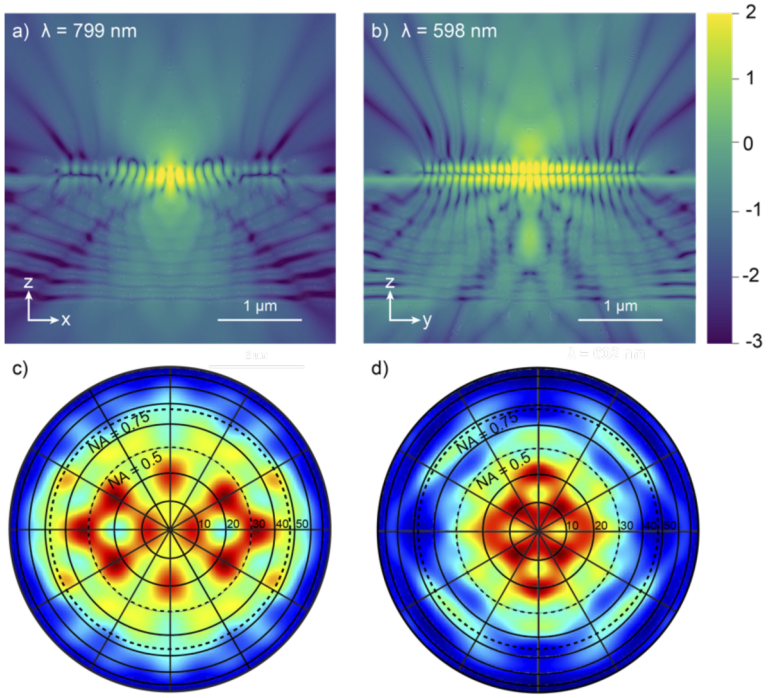

Fig. 4. Dipole emission profiles. (a, b) Cross sections of dipole emission electric field intensity at the two device resonances, plotted with a $\log_{10}$ scale. In (a) the dipole orientation is in the x-direction and in (b) the dipole orientation is in the y-direction. (c, d) Far field electric field intensity projections of upward dipole emission. (c) Far field projection for a dipole orientated in the x-direction, on resonance at the longer resonance wavelength ($\lambda = 799$ nm). (d) Corresponding projection for a dipole oriented in the y-direction, on resonance at the shorter resonance wavelength ($\lambda = 598$ nm).

3. Nanofabrication with templated atomic layer deposition (ALD) of TiO_2

The procedure used to fabricate the circular Bragg resonators is detailed in [28]. Briefly, electron beam lithography is used to define a device template into polymethyl methacrylate (PMMA), which is then filled by conformal deposition of high-index (n ~ 2.4), low-loss TiO_2 via ALD. After excess TiO_2 is removed by dry etching, the PMMA template is stripped with a wet etch (Nanostrip) and the final devices are annealed on a hot plate at 250 C for two hours.

As discussed in previous work [28], this process yields high-performance nanophotonic devices with minimal surface roughness on arbitrary substrates. It offers uniquely high integration capability because the substrate underlying the resonators is never exposed to plasma etching, and the ALD step can be performed on virtually any substrate, including two-dimensional materials which lack out-of-plane bonds [29]. To match our simulations and to demonstrate the devices' performance when interfaced with thin films, we fabricated devices on 50 nm TiO_2 films which were grown on fused silica using the same ALD process as the resonators themselves.

The scanning electron microscope (SEM) images in Fig. 5 show the fabricated dual resonance devices. Different combinations of grating period and disc radius can yield qualitatively different geometries, which can be seen by comparing Fig. 5(c) and 5(d). Because our fabrication approach is ambivalent to the device geometry, and because the critical dimensions of these devices are well above the electron beam writing resolution, we do not detect any degradation of fabrication outcomes as the structure geometry varies.

Optics EXPRESS

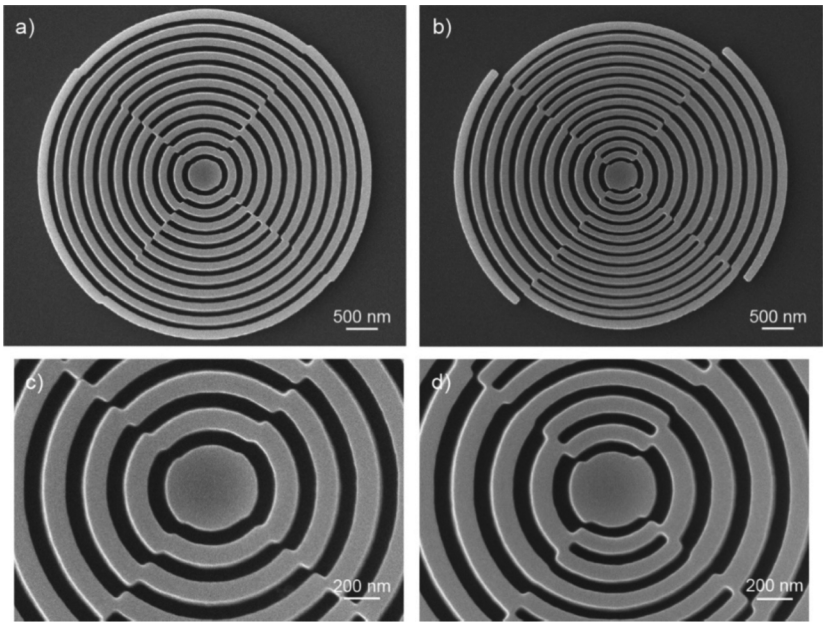

Fig. 5. Scanning electron microscopy (SEM) of fabricated dual resonance devices. (a,c) Device with parameters $(a_1, R_1) = (210, 226)$ nm, $(a_2, R_2) = (235, 250)$ nm and $\theta_1 = \theta_2 = 90°$. (b, d) Device with parameters $(a_1, R_1) = (179, 212)$ nm, $(a_2, R_2) = (235, 250)$ nm and $\theta_1 = \theta_2 = 90°$.

4. Polarized reflection spectroscopy

4.1. Experimental apparatus

We used a home-built confocal microscopy apparatus to probe the resonances of the multi-resonant devices with reflection spectroscopy. A supercontiunuum source (YSL Photonics) was focused onto the sample by an objective lens and aligned to each device using voltage-controlled galvanometer mirrors. Reflected light was collected into a spectrometer and CCD detector (300 g/mm, Princeton Instruments). A linear polarizer plus half-wave plate were used to rotate the polarization of the excitation laser. In our experiments, we measured devices which exhibit resonances in the 700–900 nm range, as this wavelength range overlaps high intensity output from the supercontinuum source and high quantum efficiency of the CCD detector used in the experiments. Because TiO_2 has a relatively large bandgap (~3.3 eV) and high index through the visible and IR ($n > 2.3$ at 1550 nm) [28], these devices can also be extended to further wavelength ranges.

4.2. Dual resonance device spectroscopy

The bullseye antenna resonances appear as asymmetric Fano lineshapes in reflection spectroscopy due to the interference of the resonator mode(s) with reflection from the underlying thin film and substrate [33]. As shown in Fig. 6, for dual resonance devices, we detect multiple resonances on top of the supercontinuum source background that vary in intensity as the excitation polarization is rotated. We note that the sharp feature near 830 nm that appears in all spectra is an artifact from the supercontinuum generation and is unrelated to the antenna devices. The three plots in Fig. 6 correspond to three different devices with varying grating periods and disc radii, which

Optics EXPRESS

yield different combinations of resonance wavelengths. As the beam polarization is varied in 15° increments from 0 to 90°, one resonance in each device becomes less intense while the other grows more intense. Comparing the spectra when the excitation beam is polarized at 0° and 90°, the polarization selectivity of each resonance is clear, and the features of these spectra agree with predictions from simulations [33]. By fitting the resonance features to Fano lineshapes, we extracted quality factors in the range 85–205, which are also in accordance with our simulated devices [33].

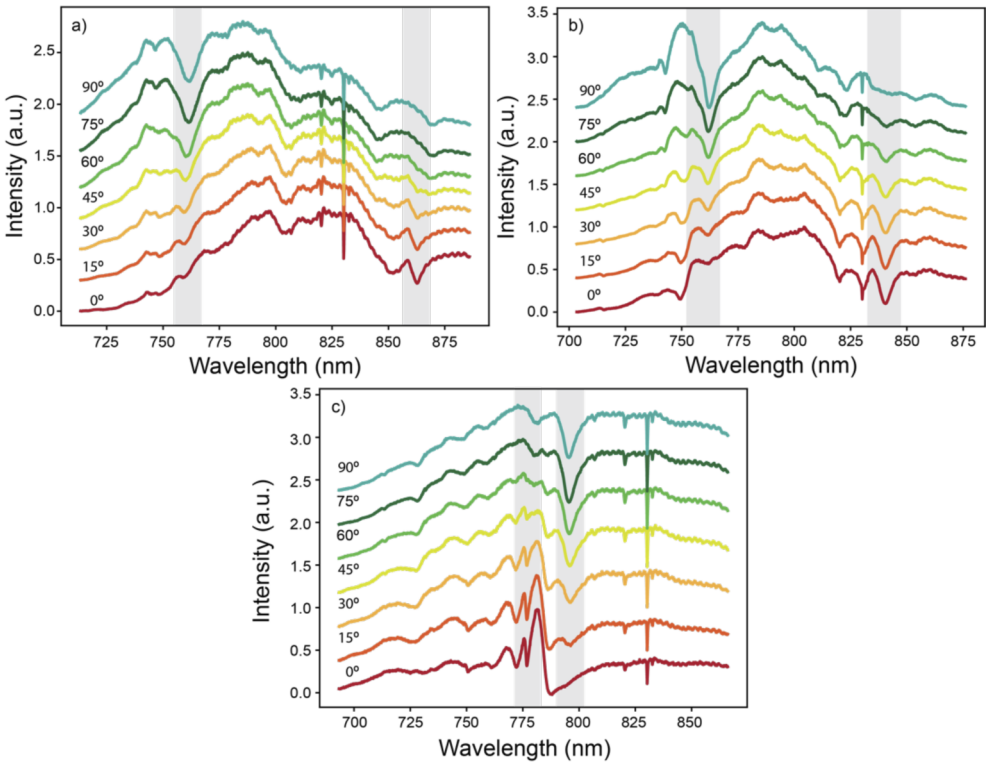

Fig. 6. Polarized reflection spectroscopy of dual resonant devices. (a-c) Reflected spectra versus beam polarization for devices with varying combinations of resonances. The data are not background subtracted, and the sharp feature near 830 nm is due to the supercontinuum source spectrum. For each device measured, $\theta_1 = \theta_2 = 90°$.

4.3. *Triple resonance devices*

Because circular Bragg resonators are rotationally symmetric, we can extend the features of dual resonance devices to devices with a larger number of resonances. To demonstrate this principle, we simulated, fabricated, and measured the reflection response of triple resonance devices. To generate a third polarization-selective resonance, we simply segment the bullseye into three, introducing a third set of grating period, central disc radius, and subtended angle parameters (a_3, R_3, θ_3).

Figure 7(a) shows the simulated electric field intensity underneath a three-resonance device as a function of incident beam polarization. In principle, the three resonances should be maximized at 0°, 60°, and 120°, respectively. However, crosstalk between the resonances skews these values slightly, which can be seen in the polar plot. The SEM images in Figs. 7(b) and 7(c) indicate that our ALD-based fabrication method can readily produce devices with three or more resonances,

Optics EXPRESS

as we do not see any defects in the TiO_2 structure. Finally, reflection spectroscopy of triple resonance devices demonstrates that we can generate three polarization-selective resonances in one structure. For the device measured in Fig. 7(d), the three resonances vary in intensity as the excitation beam polarization is rotated fully from 0° to 180°. The resonances are nominally maximized at 0°, 60°, and 120°, as anticipated.

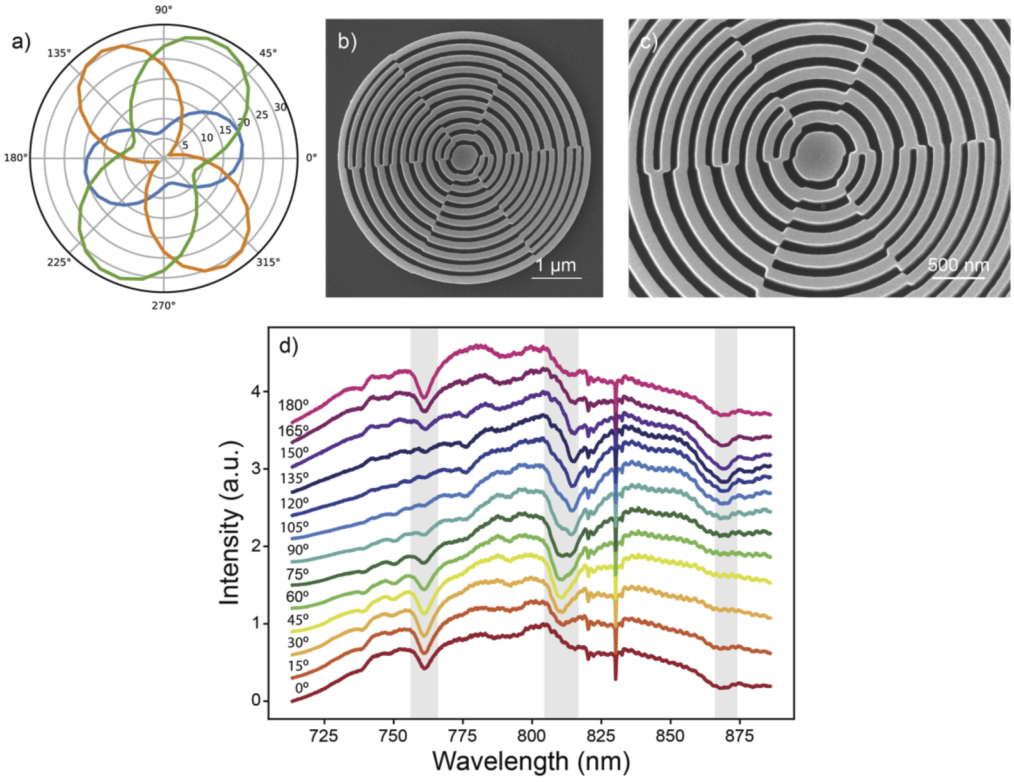

Fig. 7. Triple resonance devices. (a) Simulated beam intensity at $z = -25$ nm as a function of polarization for a device with three resonances and $\theta_1 = \theta_2 = \theta_3 = 60°$. (b, c) SEM images of a fabricated triple resonance device. (d) Reflection spectroscopy versus beam polarization for a triple resonance device with $\theta_1 = \theta_2 = \theta_3 = 60°$.

5. Conclusions

We have shown all-dielectric, multi-resonant CBR devices that combine wavelength and polarization multiplexing with the ability to efficiently direct underlying dipole emission into collection optics. The nanofabrication approach used to generate these devices offers high integration capability, making them compatible with a range of quantum and low-dimensional materials for applications in sensing and nonlinear frequency generation [36–38]. In other applications, multi-resonant CBRs may find use as ultracompact polarimeters [39] or polarization-tunable transmissive color filters [40].

Funding. University of Chicago; Boeing.

Acknowledgments. This work made use of the Pritzker Nanofabrication Facility of the Pritzker School of Molecular Engineering at the University of Chicago, which receives support from the Soft and Hybrid Nanotechnology Experimental (SHyNE) Resource (NSF ECCS-1542205), a node of the National Science Foundation's National Nanotechnology Coordinated Infrastructure. This work also made use of shared facilities supported by the NSF MRSEC Program under grant no. DMR-0820054. FDTD simulations were completed with resources provided by the University of Chicago's

Optics EXPRESS

Research Computing Center. A.B. acknowledges support from the NSF Graduate Research Fellowship under grant no. DGE-1746045 and from the Boeing company.

Disclosures. The authors declare no conflicts of interest.

Data availability. Data underlying the results presented in this paper are not publicly available at this time but may be obtained from the authors upon reasonable request.

Supplemental document. See Supplement 1 for supporting content.

References

1. T. G. Tiecke, J. D. Thompson, N. P. de Leon, L. R. Liu, V. Vuletić, and M. D. Lukin, "Nanophotonic quantum phase switch with a single atom," Nature **508**(7495), 241–244 (2014).
2. T. Zhong, J. M. Kindem, E. Miyazono, and A. Faraon, "Nanophotonic coherent light–matter interfaces based on rare-earth-doped crystals," Nat Commun **6**(1), 8206 (2015).
3. J. Xavier, D. Yu, C. Jones, E. Zossimova, and F. Vollmer, "Quantum nanophotonic and nanoplasmonic sensing: towards quantum optical bioscience laboratories on chip," Nanophotonics **10**(5), 1387–1435 (2021).
4. F. Vollmer and L. Yang, "Label-free detection with high-Q microcavities: a review of biosensing mechanisms for integrated devices," Nanophotonics **1**(3-4), 267–291 (2012).
5. E. F. Schubert, E. J. Huntm, M. Micovicr, J. Malikd, L. Sivcoa, Y. Choand G, and J. Zydzik, "Highly efficient light-emitting diodes with microcavities," Science **265**(5174), 943–945 (1994).
6. M. Pelton, C. Santori, J. Vučković, B. Zhang, G. S. Solomon, J. Plant, and Y. Yamamoto, "Efficient Source of Single Photons: A Single Quantum Dot in a Micropost Microcavity," Phys. Rev. Lett. **89**(23), 233602 (2002).
7. Y. Qi and Y. Li, "Integrated lithium niobate photonics," Nanophotonics **9**(6), 1287–1320 (2020).
8. G. Moody, L. Chang, T. J. Steiner, and J. E. Bowers, "Chip-scale nonlinear photonics for quantum light generation," AVS Quantum Sci. **2**(4), 041702 (2020).
9. S. Fathpour, "Heterogeneous nonlinear integrated photonics," IEEE J. Quantum Electron. **54**(6), 1–16 (2018).
10. S. M. Hendrickson, A. C. Foster, R. M. Camacho, and B. D. Clader, "Integrated nonlinear photonics: emerging applications and ongoing challenges," J. Opt. Soc. Am. **31**(12), 3193–3203 (2014).
11. K. Rivoire, S. Buckley, and J. Vučković, "Multiply resonant photonic crystal nanocavities for nonlinear frequency conversion," Opt. Express **19**(22), 22198–22207 (2011).
12. L. Ouyang, T. Meyer-Zedler, K.-M. See, W.-L. Chen, F.-C. Lin, D. Akimov, S. Ehtesabi, M. Richter, M. Schmitt, Y.-M. Chang, S. Grafe, J. Popp, and J.-S. Huang, "Spatially Resolving the Enhancement Effect in Surface-Enhanced Coherent Anti-Stokes Raman Scattering by Plasmonic Doppler Gratings," ACS Nano **15**(1), 809–818 (2021).
13. S. A. S. Tali and W. Zhou, "Multiresonant plasmonics with spatial mode overlap: overview and outlook," Nanophotonics **8**(7), 1199–1225 (2019).
14. S. Fossati, S. Hageneder, S. Menad, E. Maillart, and J. Dostalek, "Multiresonant plasmonic nanostructure for ultrasensitive fluorescence biosensing," Nanophotonics **9**(11), 3673–3685 (2020).
15. J. S. Levy, M. A. Foster, A. L. Gaeta, and M. Lipson, "Harmonic generation in silicon nitride ring resonators," Opt. Express **19**(12), 11415–11421 (2011).
16. P. P. Absil, J. V. Hryniewicz, B. E. Little, P. S. Cho, R. A. Wilson, L. G. Joneckis, and P.-T. Ho, "Wavelength conversion in GaAs micro-ring resonators," Opt. Lett. **25**(8), 554–556 (2000).
17. Y. Sun and X. Fan, "Optical ring resonators for biochemical and chemical sensing," Anal. Bioanal. Chem. **399**(1), 205–211 (2011).
18. X. Guo, C.-L. Zou, C. Schuck, H. Jung, R. Cheng, and H. X. Tang, "Parametric down-conversion photon-pair source on a nanophotonic chip," Light: Sci. Appl. **6**(5), e16249 (2017).
19. L. Ateshian, H. Choi, M. Heuck, and D. Englund, arxiv:2009:13029.
20. R. Jordan, D. G. Hall, O. King, G. Wicks, and S. Rishton, "Lasing behavior of circular grating surface-emitting semiconductor lasers," J. Opt. Soc. Am. B **14**(2), 449–453 (1997).
21. C. Bauer, H. Giessen, B. Schnabel, E.-B. Kley, C. Schmitt, U. Scherf, and R. F. Mahrt, "A Surface-Emitting Circular Grating Polymer Laser," Adv. Mater. **13**(15), 1161–1164 (2001).
22. S. Schönenberger, N. Moll, T. Stöferle, R. F. Mahrt, B. J. Offrein, S. Götzinger, V. Sandoghdar, J. Bolten, T. Wahlbrink, T. Plötzing, M. Waldow, and M. Först, "Circular Grating Resonators as Small Mode-Volume Microcavities for Switching," Opt. Express **17**(8), 5953–5964 (2009).
23. L. Li, E. H. Chen, J. Zheng, S. L. Mouradian, F. Dolde, T. Schröder, S. Karaveli, M. L. Markham, D. J. Twitch, and D. Englund, "Efficient Photon Collection from a Nitrogen Vacancy Center in a Circular Bullseye Grating," Nano Lett. **15**(3), 1493–1497 (2015).
24. H. Wang, "Towards optimal single-photon sources from polarized microcavities," Nat. Photonics **13**(11), 770–775 (2019).
25. N. M. H. Duong, Z.-Q. Xu, M. Kianinia, R. Su, Z. Liu, S. Kim, C. Bradac, T. T. Tran, Y. Wan, L.-J. Li, A. Solntsev, J. Liu, and I. Aharonovich, "Enhanced Emission from WSe2 Monolayers Coupled to Circular Bragg Gratings," ACS Photonics **5**(10), 3950–3955 (2018).
26. B. Chen, Z. He, Z.-J. Liu, Y.-K. Wang, Y.-N. Gao, I. Aharonovich, Z.-Q. Xu, and J. Liu, "Simultaneously enhanced linear and nonlinear photon generations from WS2 by using dielectric circular Bragg resonators," Nanophotonics **9**(8), 2587–2592 (2020).

Optics EXPRESS

27. E. De Leo, A. Cocina, P. Tiwari, L. V. Poulikakos, P. Marques-Gallego, B. le Feber, D. J. Norris, and F. Prins, "Polarization Multiplexing of Fluorescent Emission Using Multiresonant Plasmonic Antennas," ACS Nano **11**(12), 12167–12173 (2017).
28. A. Butcher, X. Guo, R. Shreiner, N. Delegan, K. Hao, P. J. Duda, D. D. Awschalom, F. J. Heremans, and A. A. High, "High-Q Nanophotonic Resonators on Diamond Membranes using Templated Atomic Layer Deposition of TiO2," Nano Lett. **20**(6), 4603–4609 (2020).
29. R. Shreiner, K. Hao, A. Butcher, and A. A. High, "Electrically controllable chirality in a nanophotonic interface with a 2D semiconductor," Nat. Photonics *In Press* (2022).
30. X. Guo, N. Delegan, J. C. Karsch, Z. Li, T. Liu, R. Shreiner, A. Butcher, D. D. Awschalom, F. J. Heremans, and A. A. High, "Tunable and Transferable Diamond Membranes for Integrated Quantum Technologies," Nano Lett. **21**(24), 10392–10399 (2021).
31. N. Moll, T. Stöferle, S. Schönenberger, and R. F. Mahrt, "Ultra-high quality-factor resonators with perfect azimuthal Modal-Symmetry," Opt. Express **17**(23), 20998–21006 (2009).
32. S. Banerji, M. Meem, A. Majumder, F. Guevara Vasquez, B. Sensale-Rodriguez, and R. Menon, "Imaging with flat optics: metalenses or diffractive lenses?" Optica **6**(6), 805–810 (2019).
33. Supplementary Information.
34. L. Li, H. Choi, M. Heuck, and D. Englund, "Field-based design of a resonant dielectric antenna for coherent spin-photon interfaces," Opt. Express **29**(11), 16469–16476 (2021).
35. S. Molesky, Z. Lin, A. Y. Piggott, W. Jin, J. Vuckovic, and A. W. Rodriguez, "Inverse design in nanophotonics," Nat. Photonics **12**(11), 659–670 (2018).
36. S.-H. Oh, H. Altuh, X. Jin, T. Low, S. J. Koester, A. P. Ivanov, J. B. Edel, P. Avouris, and M. S. Strano, "Nanophotonic biosensors harnessing van der Waals materials," Nat Commun **12**(1), 3824 (2021).
37. K. L. Seyler, J. R. Schaibley, P. Gong, P. Rivera, A. M. Jones, S. Wu, J. Yan, D. G. Mandrus, W. Yao, and X. Xu, "Electrical control of second-harmonic generation in a WSe_2 monolayer transistor," Nat. Nanotechnol. **10**(5), 407–411 (2015).
38. J. Hernandez-Rueda, M. L. Noordam, I. Komen, and L. Kuipers, "Nonlinear Optical Response of a WS_2 Monolayer at Room Temperature upon Multicolor Laser Excitation," ACS Photonics **8**(2), 550–556 (2021).
39. V. Vashistha, G. Vaidya, P. Gruszecki, G. Vaidya, P. Gruszecki, A. E. Serebryannikov, and M. Krawczyk, "Polarization tunable all-dielectric color filters based on cross-shaped Si nanoantennas," Sci. Rep. **7**(1), 8092 (2017).
40. A. Martinez, "Polarimetry enabled by nanophotonics," Science **362**(6416), 750–751 (2018).